High-speed imaging of vapor plume in the treatment of dissimilar Aluminum/Titanium interface with Yb:YAG laser pulse

Manoj Raja Kumar, Iryna Tomashchuk, Jean-Marie Jouvard, Mélanie Duband

To cite this version:

Manoj Raja Kumar, Iryna Tomashchuk, Jean-Marie Jouvard, Mélanie Duband. High-speed imaging of vapor plume in the treatment of dissimilar Aluminum/Titanium interface with Yb:YAG laser pulse. Journal of Advanced Joining Processes, 2022, 5, pp.100097. 10.1016/j.jajp.2022.100097 . hal-04840453

HAL Id: hal-04840453
https://hal.science/hal-04840453v1

Submitted on 19 Dec 2024

HAL is a multi-disciplinary open access archive for the deposit and dissemination of scientific research documents, whether they are published or not. The documents may come from teaching and research institutions in France or abroad, or from public or private research centers.

L'archive ouverte pluridisciplinaire **HAL**, est destinée au dépôt et à la diffusion de documents scientifiques de niveau recherche, publiés ou non, émanant des établissements d'enseignement et de recherche français ou étrangers, des laboratoires publics ou privés.

Distributed under a Creative Commons Attribution - NonCommercial 4.0 International License

Version of Record: https://www.sciencedirect.com/science/article/pii/S2666330922000036
Manuscript_8a643ba68d987536c4b0a73c20320211

High-Speed Imaging of Vapor Plume in the treatment of Dissimilar Aluminum/Titanium Interface with Yb:YAG Laser Pulse

Manoj Raja-Kumar, Iryna Tomashchuk*, Jean-Marie Jouvard, Mélanie Duband

Laboratoire Interdisciplinaire Carnot de Bourgogne, UMR CNRS-6303, Université de Bourgogne Franche-Comté, 12 rue de la Fonderie, 71200 Le Creusot, France.

*iryna.tomashchuk@u-bourgogne.fr

Abstract

It is ideal to observe the vapor plume to have a better understanding of the keyhole dynamics in dissimilar laser welding. This work is dedicated to the high-speed imaging and spectroscopic analysis of the vapor plume and post-mortem analysis of melted zone produced from the interaction of a 6 ms Yb:YAG laser pulse with the aluminum A5754 - titanium T40 interface. These experiments are performed for different offsets of the laser spot from the joint line. The high-speed imaging is performed at two different wavelength (infrared 810 nm and ultraviolet 394 nm) regions. Morphological characteristics such as dimensions and orientation of the plume are studied and compared. The laser spot position affects the angle of inclination. It is observed that the plume inclines towards the aluminum side. The observation of inclination varies with the recording wavelength. The interrelationship between the inclination of the vapor plume and the laser spot position for a chosen observation wavelength is not self-explanatory. Post-mortem observation and EDX analysis of the melted zone, are correlated with the results from high-speed imaging. Spectroscopic analysis of the vapor plume associated with the Boltzmann linearization for temperature calculation, provides confirmation on the existing correlations between results from high-speed imaging and post-mortem analysis.

Keywords: laser welding, vapor plume, dissimilar welding, high-speed imaging, plume spectroscopy.

© 2022 published by Elsevier. This manuscript is made available under the CC BY NC user license
https://creativecommons.org/licenses/by-nc/4.0/

List of Abbreviations

HSI – High Speed Imaging

TER – Thermally Excited Region

AER – Atomically Excited Region

LSP – Laser Spot Position

F.HEIGHT – Feret's Maximum Diameter

F.WIDTH – Feret's Minimum Diameter

E.HEIGHT – Ellipse Major axis

E.WIDTH – Ellipse Minor axis

PZ – Probability Zones

EDS – Energy-dispersive X-ray spectroscopy

λ - Wavelength

1 Introduction

In deep penetration laser welding, the laser-matter interaction produces a keyhole in which the vaporization of the metals occurs. Analysis of the vapor plume that is emitted from the keyhole by different methods allows obtaining an important information about the phenomenology of laser welding and opens the possibilities of process control. The observation of the vapor plume and the melt pool during Nd:YAG laser continuous welding of steel using high speed imaging (HSI) in a spectral range of 450 – 930 nm allowed establishing the correlation between the angle of the inclination of the plume and the dynamics of the keyhole walls (Fabbro et al., 2006). Shcheglov et al., 2013 performed the study of laser-induced plume attenuation of a probe 1.3 µm radiation as well as of continuous radiation in the 250–600 nm region and demonstrated that the vapor plume dynamics was an indicator of spattering and instabilities in the welding process. HSI of the vapor plume of 5083 Al-alloy at $\lambda = 350 - 950$ nm combined with particle velocimetry was used to correlate the plume velocity with keyhole dimensions and collapse (Huang et al., 2020). Li et al., 2021 demonstrated the correlation between the keyhole stability and the dynamics of the plume using high speed imagining with 808 nm bandpass filter. White light illuminated plume observed in the fiber laser welding of steel distinguished the plume to contain two zones: the oscillating part and the slender central part (Zou et al., 2021).

In case of laser welding of dissimilar materials, the study of vapor plume is of particular interest as it brings the insight to the intermixture dynamics that is essential for the weld quality. Schmalen and Plapper, 2018 investigated the possibility of using laser-induced plume spectroscopy for the intermixture detection during continuous overlap welding between aluminum and copper. The involvement of the lower material (copper) in the melted zone could be controlled basing on the emission intensity on a material-specific wavelength. A method of intermixture detection based on a set of two couples of photodiodes corresponding to Al- and Cu-specific wavelength regions respectively was proposed. Seibold et al., 2020 demonstrated the possibility of process control with real-time pulse shaping during overlap laser welding of aluminum/copper and aluminum/steel combinations. In contrast to the previous study, the correlation between the intensity of 485 nm diode signal corresponding to AlO emission (which is common for two studied couples) and the whole process dynamics was demonstrated, instead of comparing the emission intensities of two material-specific wavelengths.

In the present research, the combination of high speed imaging with emission spectroscopy and post-mortem analysis is used to elucidate the phenomenology of plume behavior during Yb:YAG laser pulse on dissimilar titanium/aluminum alloy interface in butt configuration. In the previous work (Raja Kumar et al., 2020 a), this approach was applied to the continuous dissimilar welding of titanium T40 and aluminum A5754 alloy, and the plume was observed using 810 nm bandpass filter. Then, a pulsed laser welding of these materials was investigated using the same approach (Raja Kumar et al., 2021). In both studies, the plume inclination towards aluminum side was observed, which was attributed to the action of the titanium vapor jet. The spectral region of 810 nm corresponds to the thermal emission only, as it does not contain any element-specific emission lines. In the present study, it was decided to compare the plume imagery from this thermal emission region with an imagery based on atomic emission region. From the NIST database (Kramida et al., 2020), we know that both Ti I and Al I strongly emit at the 394 nm wavelength regime. Comparison of HSI at this wavelength of atomic emissions ($\lambda = 394$ nm) to the continuous thermal emissions at ($\lambda = 810$ nm) could reveal more details about the vapor plume structure and dynamics. Hence, in this work, the plume induced by Yb:YAG laser pulse at the interface between commercially pure titanium T40 and A5754 aluminum alloy was studied using HSI with 394 nm and 810 nm bandpass filters. Correlations were made between HSI image treatment results, plume spectroscopy and post-mortem analysis of the impact zones.

2 Experimental setup and procedures

2.1 Laser and welding materials

TruDisk 6001 by Trumpf, a Yb:YAG (λ = 1030 nm) continuous near-Gaussian laser source was used to produce 6 ms laser pulses with a power of 2 kW and a spot diameter of 600 µm. T40 commercially pure titanium and A5754 aluminum alloy plates were welded in butt configuration (Figure 1.A). The laser was focused from above at 3° angle from the vertical axis (to avoid back reflection into the laser head) to the top surface of the 3 mm thick metal plates. The experiments were done at atmospheric conditions and no protective gas flow was used. The experiments were performed with 5 different laser spot positions with respect to the joint line (positions of center of beam: $\Delta_{-0.2}$ = 0.2 mm on Al, $\Delta_{-0.1}$ = 0.1 mm on Al, Δ_0 = Joint line, $\Delta_{+0.1}$ = 0.1 mm on Ti, $\Delta_{+0.2}$ = 0.2 mm on Ti) as shown in Figure 1.B. Negative values indicate the beam towards the aluminum side, while the positive values indicate beam offset towards the titanium side. All the experiments were repeated multiple times to have a bigger sample size and the beam offsets were performed to understand the competitive vaporization of the two materials.

2.2 High speed imaging

2.2.1 Image acquisition

A high-speed camera Phantom v9.1 (1000 fps at full resolution 1632x1200 pixels) with a CMOS sensor was used to record the images of the vapor plume from the front (Figure 1.A). The camera was used with a Nikon AF Micro-Nikkor 200mm f/4D IF-ED telescopic lens at 65 centimeters (working distance) from the laser spot position. Instead of using a perfectly horizontal position for the camera in alignment with the plane of the impact surface of the metals, a small angle (<5°) was introduced for two reasons.

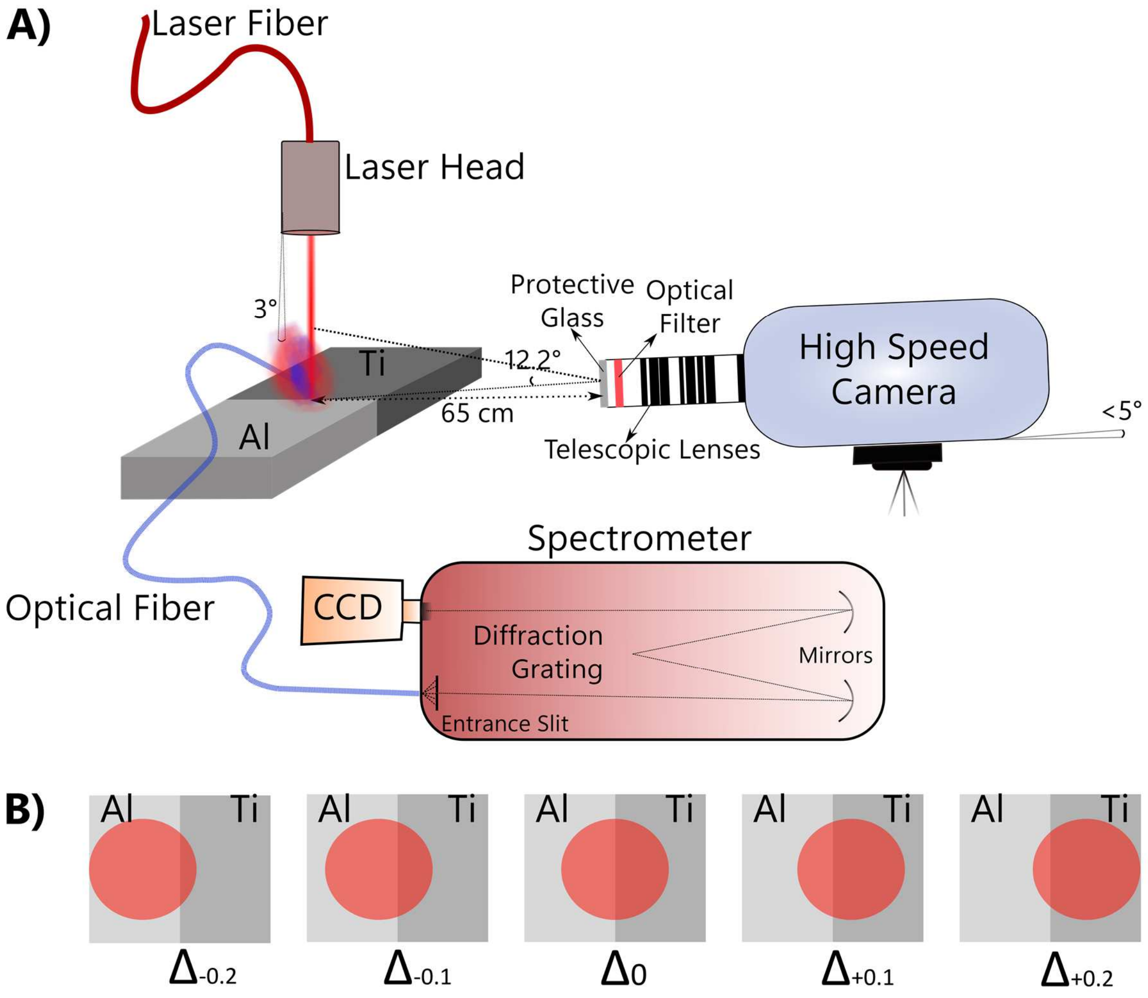

Figure 1: A) Schematic of the experimental setup. B) Laser Spot positions.

1. To have a view of the joint line for better positioning the point of impact to the horizontal center of the captured images.
2. To reduce the Bokeh effect and the loss of quality due to reduction in transmission of the lens system near the edges.

2 different optical band pass filters were used during the experiments, 810 ± 3 nm, and 394 ± 3 nm with full width at half maximum 10 ± 2 nm. All the captures were made with the frame rate 6400 fps with the resolution of 480 x 480 pixels and the exposure time of 120 µs. The physical dimension of the zone of capture was 15 mm x 15 mm. The aperture index of the

telescopic lens system was set to 11 for all the experiments. The picture angle of the lens system is 12.20°, the depth of field = 3 mm and a reproduction ratio 1/1.7.

Although the experiments were made under different conditions of laser spot position and the videos were captured through different optical filters, the parameters of the camera were conserved so that all the videos can have consistent data for the process of image treatment and statistical analysis. But the drawback of not changing the camera parameters by adapting to the visual output of the experiments and the optical filters, can lead to loss of critical information in the images. In this work, such losses are partially compensated through image processing (section 2.2.2). In the scope of this article, this drawback is not addressed along with the influence of the absorption values of the lens setup and the spectral response[*] of the optical components in the camera.

2.2.2 Image processing

A total of 71 dissimilar welding videos were captured. 31 videos were captured with 394 nanometer filter and 40 videos were captured with 810 nm filter. All these videos were stacks of 8-bit grayscale images. Fiji (Schindelin et al., 2012) is the software application that was used in the image treatment and analysis. The videos contain numerous unnecessary elements which could intervene in the data acquisition process. Each video which was filmed for different experimental conditions under different wavelength regimes, contains multiple images, and each image contains multiple data sets. Therefore, image processing becomes a necessity and needs to be automated. The steps taken in the image processing are described in the order of execution.

---

[*] Phantom v9.1 camera spectral and color response is available at:

http://service.phantomhighspeed.com/Documentation/Support By Model Pages/Phantom V9.1/PHANTOM_V9.1_spectral_and_color_response_rev_7.pdf

First, to avoid the issue of loss in quality for the videos and reduce the uncertainties in the data sets, normalization of the entire stacks is performed by the “Enhance Contrast” function using the default value of ‘0.3 % for saturated pixels’ while taking into account, the stack histogram. An example of the image after normalization can be seen in the Figure 2.A.

Since the videos included a part of the metallic plates and the melted zone, the plume reflected on the metal plates had to be removed. For the Phantom v9.1 camera’s sensor, the black reference had to be done manually by closing the filter attachment in front of the objective with the ‘62 mm snap-on front lens cap’. This process, no matter how carefully done could exert small forces on the camera thereby displacing the zone of capture. And so, the videos were cropped manually to remove the reflections of the vapor from the metal plates (Figure 2.B). Since the cropping was done manually, an uncertainty of 5 to 10 pixels is introduced into the height and other related characteristics of the vapor plume.

In the previous work (Raja Kumar et al., 2021), some primary characteristics such as the plume height, plume width, etc. were discussed. But in-depth analysis of the HSI observations required revision of the methodology used to study. We identify the different parts of the plume – the vapor intense regions, the highly diffuse regions, the mildly diffuse regions, turbulences in the intense or mildly diffuse regions, regions illuminated by electronic background noise, edge bleeding effects (Levesque & Buteau, 2007), spatters (Kaplan & Powell, 2011), motion blur (Sunghyun et al., 2007), etc. The exposure time of 120 µs applied to the moving plume envelop leads to the motion blur over several pixels. This is one of the main difficulties in determining the exact outer edge of the plume.

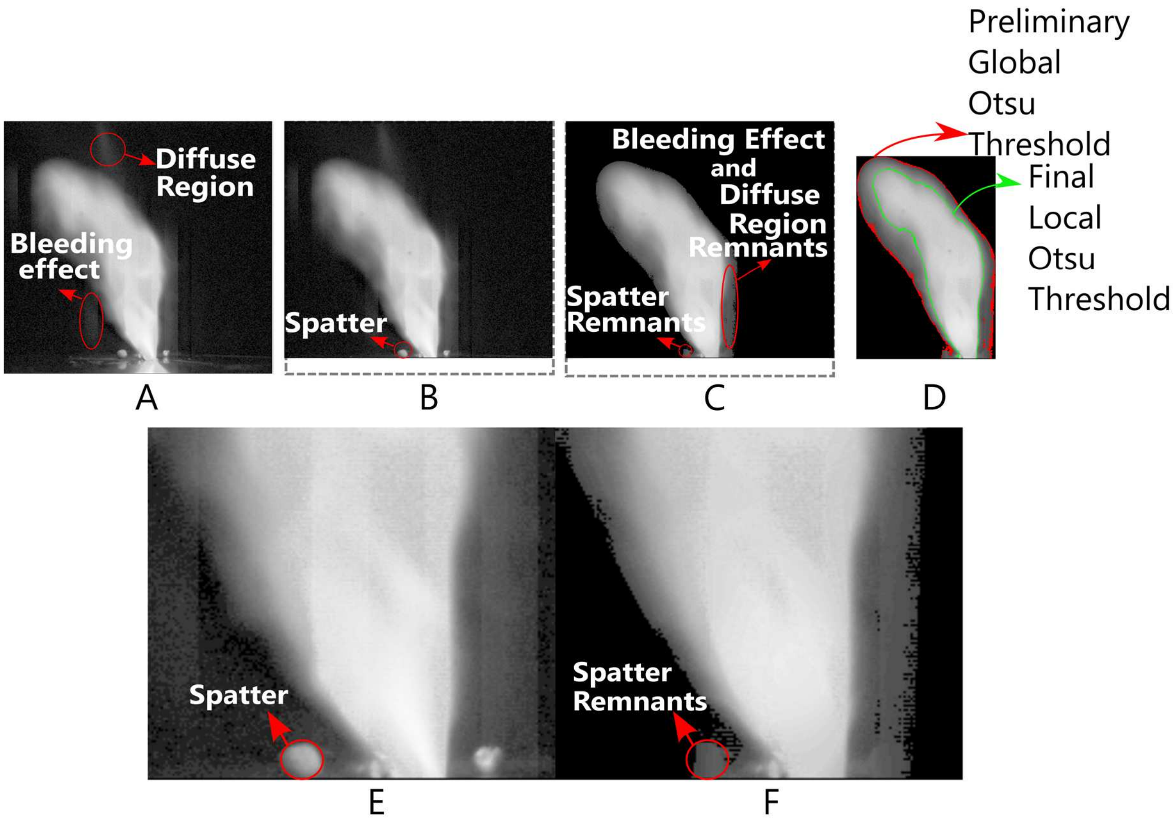

Figure 2: Image processing methodology: A) Normalization, B) Cropping, C) Noise Removal D) Multi-level thresholding, E) Zoomed Spatter and F) Zoomed spatter remnants.

In this work, we analyze the plume and since we are using optical filters in different wavelengths, the highly diffuse regions, spatters, and noise need to be removed. This process is done by auto-thresholding of the stack of images using the Otsu method (Otsu, 1979). The regions lying below the threshold value are cleared (Figure 2.C). The spatters were treated as outliers and were removed using the “Remove Outliers” function with a threshold value of 5 and a radius of 30 pixels. The Remove Outliers function replaces a pixel by the median of the pixels in the surrounding if it deviates from the median by more than a certain value (Schindelin et al., 2012).

Although, these steps have been performed, some unwanted data remain. For example, in the Figure 2.C, we can still see some remnants left in the place of the spatter and the bleeding effect. To eliminate these regions of unwanted bright pixels, we follow a non-destructive method of image treatment. The logic behind the choices in this image treatment step is explained as follows. We are trying to distinguish the plume region from the background noise or other unwanted effects. And since our object (plume) is large enough relative to the size of our image, we see it exhibits a bimodal distribution when we look at the histograms of both the stacks and the individual images. While a single video that has constant experimental conditions can be considered as a class, each image captured within the duration of the exposure time forms a class of its own. Therefore, utilizing the intraclass variances within the video, a global threshold using the stack histogram, the Otsu thresholding method is applied on each image to create a selection which distinguishes our initial Region of Interest (ROI) from the background (Marked red in Figure 2.D). And then, within the ROI, a local Otsu threshold is applied to create another selection. This second selection is considered as the final ROI in the plume (Marked green in Figure 2.D), and it is analyzed after setting the scale in millimeters to match the real-world physical dimensions of our image. This three-level thresholding process eliminates every possible irrelevant data from our calculations about the vapor plume which have been introduced from the experiments or the digital normalization process. In addition, the global thresholding step followed by the local thresholding conserves maximum plume data without compromising on the noise removal. And most importantly, such rigorous treatment to remove the background noise while preserving the image without binarization lets us use image moments to perform statistical analysis. The limitation of using this methodology is that, if there are images which contain very small ROI (less than 5 pixels in diameter) which indicate the start of the plume, such images are eliminated from the calculations since creating selections and analyzing in that size could not be done in Fiji without directly writing our own program for creating a selection.

Statistical tools can be used for efficient analysis of the plume data. Various such techniques have been used in the research of flame behavior (De et al., 2018) and in other fields (Farrell et al., 1994). The application of image moments could be very useful to describe/compare different trends in the spatial distribution of the vapor plume. The different types of image moments are explained (Awcock & Thomas, 1995). Some of these image moments which we have used in this article to understand the spatial distribution of the vapor plume are Area, Centre of Mass, and Centroid. They are calculated from the pixel gray value (brightness). It is important to note that, the rapidly evolving vapor plume images are very different from one frame to the next. And so, some limits exist in the usage of these statistical analysis tools. The two predominant examples that were observed from this work are, 1) variances between the calculated values could be very high depending upon the stability of the vapor plume and, 2) the temporal behavior of the plume could not be very well-defined using these tools.

2.3 Spectroscopic acquisitioning

Spectral analysis of vaporized matter was performed using an atomic emission spectrometer. The spectrometer is composed of a Czerny-Turner McPherson type monochromator - model 209 attached with an ICCD Princeton PIMAX-1K-RB camera (CCD size 1024 lines x 1024 pixels, frequency 1 MHz, pixel size 13 x 13 µm, spectral range 195-920 nm, minimum gate 2 ns). The 1.33m focal length monochromator is equipped with a 2400 lines / mm grating blazed at 250 nm. The collection and guidance of the light from the plasma to the spectrometer is carried out by an optical fiber. An optical system made up of 2 lenses L_1 with focal length 40 cm and L_2 with focal length 10 cm (magnification = 4) allows signal acquisition from the plume and its transfer into the optical fiber (core diameter 230 µm) up to at the entrance slit of the spectrometer. The sighting system is arranged perpendicular to the laser beam. The area observed corresponds to a disc with a radius of 0.5 mm centered at 1 mm from the surface of the sample. The spectral signal is integrated over the period of the laser pulse. It is therefore necessary to subtract the ambient noise from the signal.

Wavelength calibration is performed using a Hg vapor lamp. In this configuration, the spectrometer allows signal acquisition over a spectral region of approximately 3.5 nm. Intensity calibration is necessary to be able to effectively compare spectra obtained over different wavelength ranges, as the detector response varies with the wavelength range. Intensity calibration with a halogen reference source (DH 2000 Ocean Optics lamp) is applied to the spectra before analyzing them to allow spectra comparison obtained over different wavelength ranges.

Halogen reference source is calibrated in spectral irradiance $E_{ref}(\lambda)$. For each spectral region studied, we recorded the spectrum of the calibration lamp. The calibrated spectrum $E(\lambda)$ is then obtained by making the ratio of the studied spectrum $I_{sp}(\lambda)$ to the reference spectrum $I_{ref}(\lambda)$ of the calibration lamp:

$$E(\lambda) = \frac{I_{sp}(\lambda)}{I_{ref}(\lambda)} . E_{ref}(\lambda) \tag{1}$$

where $I(\lambda)$ being the difference signal - noise.

Thus, all the parts of the spectral acquisition system which have a response function such as the lens system, the optical fiber, the camera have been considered in this calibration method. As the spectrometer is not synchronized with the laser and the HSI camera and is manually operated, the acquisition is integrated over the lifetime of the plume.

2.4 Postmortem observation of the melted zone.

25 impact zones were observed post-mortem using a scanning electron microscope JSM-6610 (Jeol). Elemental mapping of the top surface of these melted zones was performed using Energy-dispersive X-ray spectroscopy (EDS) to analyze the Al (in red), Mg (in green) and Ti (in blue) distribution (Figure 3a). The additional characterizations of the melted zone are available in the **Supplementary data file**. The black vertical zone visible on the X-maps

presented on the Figures 3 and 7 is an artefact is related to the inclination angle of EDX probe with respect to the surface of the sample. The simultaneous observation made with secondary electrons SEM imagery (Figure 3b) shows that the gap between the plates is absent.

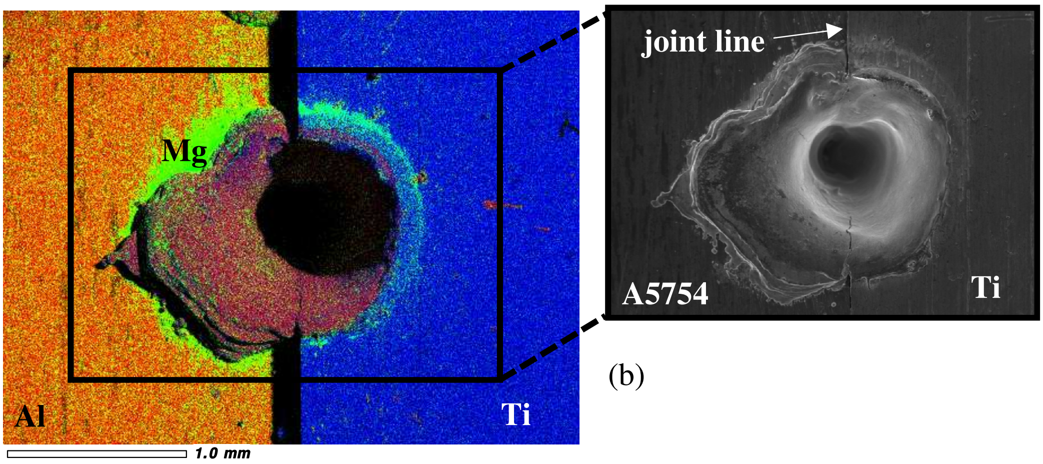

(b)

(a)

Figure 3: X-mapping (a) and secondary electrons SEM image (b) of melted zone surface (Δ_0).

3 Results and analysis

3.1 Spectral characteristics of the vapor plume

Neutral titanium (Ti I) has many emission lines distributed over the entire wavelength range. We can distinguish a weak ionization corresponding to a few Ti II lines. But the temperatures are not high (7000K), which represents vaporization of the molten material and not laser ablation plasma. Spectral analysis showed that the Al I transitions are weak and at the level of the background noise. Only the fundamental transitions at [394 – 396] nm are strong, but these two lines are self-absorbed (Surmick & Parigger, 2017). The molecular bands of AlO were observed in the region between 440 and 570 nm, which is in agreement with the results of Peuker et al., 2013, Gao et al., 2015 and Schmalen & Plapper, 2018. The magnesium present in the A5754 alloy (2-3% weight) allow to obtain lines which can be easily observed in the analysis. In the region [381-384.5] nm, we can use the Mg I line at 382.94 nm (Kurucz, 1995), line isolated and not convoluted with a titanium line. This line is characteristic of the presence of the elements composing the aluminum alloy. It will therefore be used subsequently (Figure 6) to characterize the presence of aluminum in the zone irradiated by the laser.

In this work, three spectral regions [381-384.5] nm, [393.5-397] nm and [463.5-467] nm were mainly studied. The region [393.5-397] nm corresponds to the spectral domain at which HSI was performed with the optical filter λ = 394 nm, in which two self-absorbed fundamental lines of aluminum (394.40 nm and 396.15 nm) and intense lines of titanium are present (Figure 4). In this region, we observe the simultaneous presence of aluminum and titanium whatever the offset of the laser beam with respect to the joint. Previously, Mohanta et al. 2019 also reported the simultaneous observation of Al I and Ti I lines in this region during direct 1070 nm laser melting of Ti-6Al-4V.

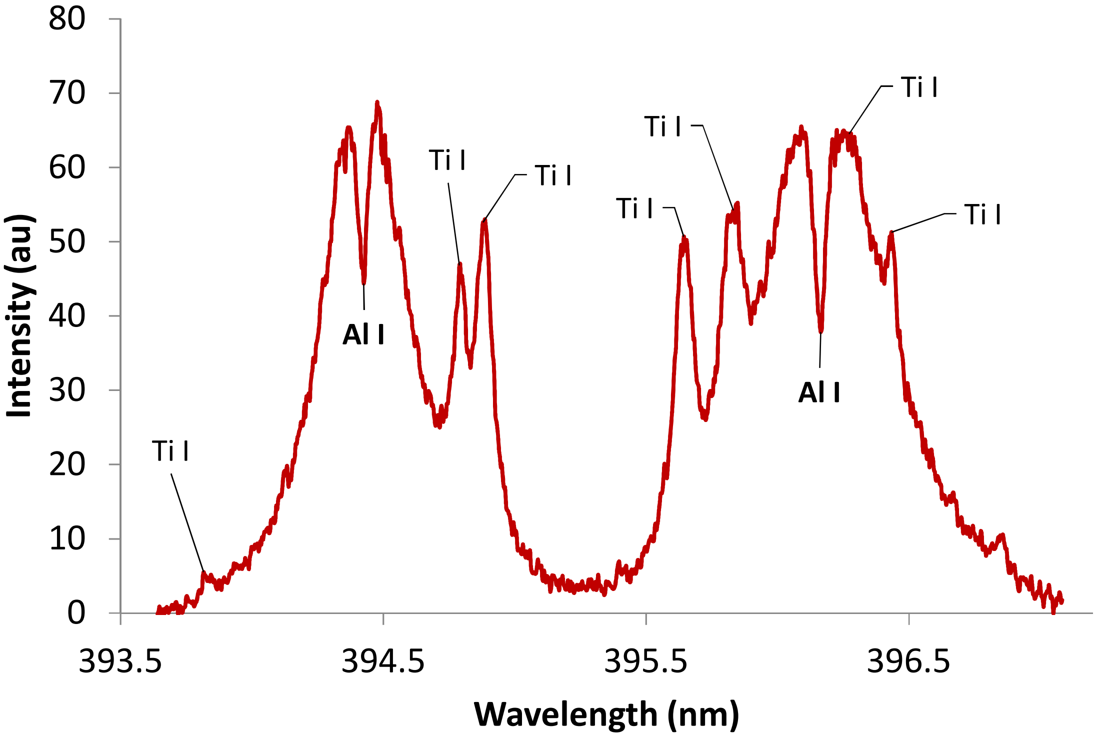

Figure 4: Al and Ti atomic transitions in the wavelength regime of the 394 optical filter for LSP $\Delta_{-0.2}$.

The other two regions are chosen for (Ti I) temperature estimation using the Boltzmann plot method. Boltzmann statistics states that the population of the energy levels of the excited atoms depends on the temperature.

$$I = \frac{N_0}{Z_T}.e^{-\frac{E}{k.T}}.g.A_{si}.h.\nu \qquad (2)$$

The method is based on the representation of the graph of $ln\left(\frac{\lambda.I}{g.A_{si}}\right)$ in function of $-\frac{E}{k.T}$. The slope of the line makes it possible to estimate the temperature T.

To apply this method, it is necessary to measure the intensity of the lines studied (after calibration and noise subtraction (section 2.3). Line profile fit is performed using PeakFit software (Systat Software, San Jose, CA). We observe the superposition of a continuous spectrum corresponding to thermal radiation and atomic emission lines.

The selected atomic transitions (Table 1) satisfy multiple criteria: separate emission lines, not self-absorbed, having a correct signal-to-noise ratio and representative of the range of energy of the upper level. Line profile adjustments allow determination of the position and intensity of the emission lines.

Table 1: Titanium lines used for atomic temperature estimation (Kurucz, 1995).

λ (nm)	**g.A (s^{-1})**	**E_i (cm^{-1})**	**J_i**	**E_s(cm^{-1})**	**J_s**
381,327	9,513E+07	16817,16	1	43033,94	1
381,486	1,205E+08	16875,12	2	43080,96	2
382,202	3,150E+08	17075,26	4	43231,99	4
383,677	4,753E+08	19573,97	4	45630,18	5
384,162	2,517E+07	11531,76	2	37555,06	3
464,519	8,568E+07	13981,77	1	35503,40	0
465,001	7,926E+07	14028,43	2	35527,75	1
465,647	1,390E+07	0	2	21469,49	3
466,758	1,958E+07	170,134	3	21588,49	4

λ – emission wavelength, g – statistical weight, A – spontaneous emission probability, Ei and Es are energy of lower and upper levels respectively, Ji and Js are angular momentums of lower and upper levels, respectively.

The Boltzmann plot method shows that the excitation temperatures of titanium are similar for all LSP (Figure 5) and are comprised between 6000 and 7000 K, which is close to the maximal temperature of 6000 K obtained by Mohanta et al., 2019 during direct 1070 nm laser melting of Ti-6Al-4V. The intensity of a line depends on both the temperature T (population of excited atoms for a given atomic level) and the total number of atoms present in the observed plume (Equation 1). Therefore, the difference in line intensities for the various LSPs does not result from a temperature difference, but rather from the difference in the amount of vaporized material.

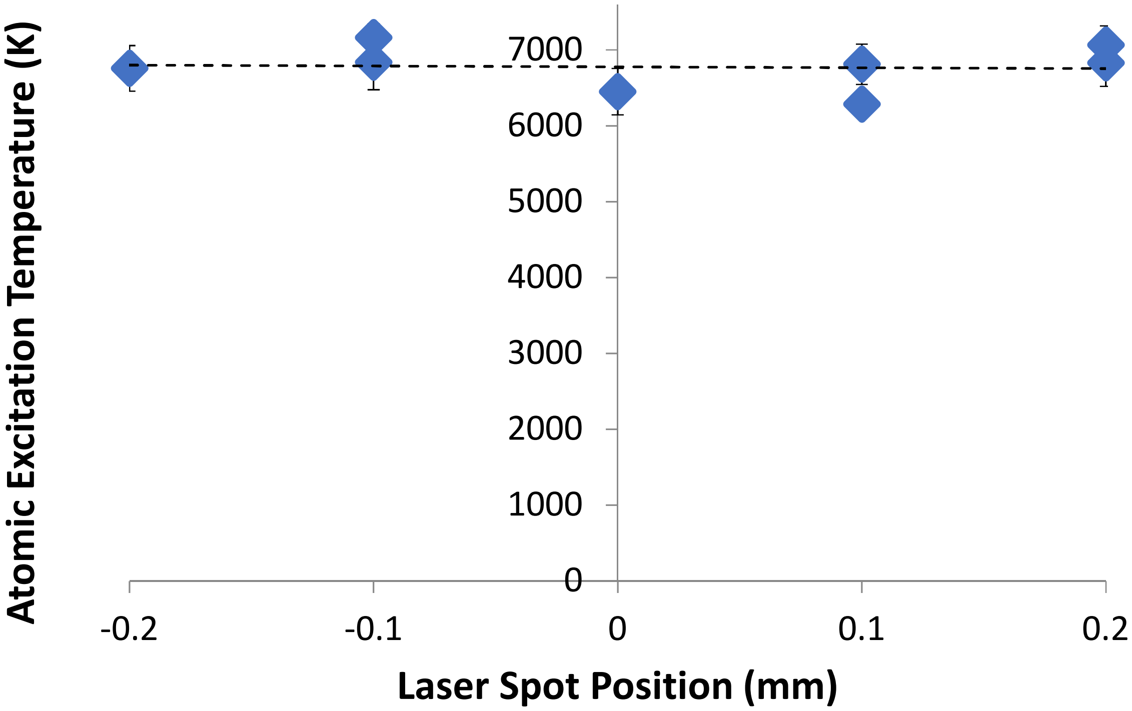

Figure 5: Atomic excitation temperature evolution with respect to LSP.

When multiple spectra were acquired for each LSP, some fluctuations were observed between different laser pulses.

- For $\Delta_{-0.2}$, some spectra did not have any titanium lines (Figure 6). In this case, we observe only magnesium lines in the region [381-384.5] nm and we observe a molecular band of AlO ($B^2\Sigma^+$ - $X^2\Sigma^+$) in the region [463.5-467] nm.

- For the LSPs $\Delta_{-0.1}$, Δ_0 and $\Delta_{+0.1}$, the intensity of the titanium and magnesium lines increase proportional to the shift of the LSP towards titanium. Such behavior is due to an increase in the amount of material vaporized (Figure 6).

- For $\Delta_{+0.2}$, the emissions from the amount of vaporized material from the aluminum alloy begin to decrease, since most of the laser is focused on titanium (Figure 6).

The intensity variation of Mg line reflects the contribution of A5754 side of the joint to the vaporization process under laser beam radiation. When the beam irradiates only the aluminum alloy, the intensity of Mg vaporization is controlled by the temperature of keyhole walls that should be close to that of aluminum. When the laser spot is progressively shifted on titanium, the temperature of the keyhole walls increases due to the higher vaporization temperature of Ti. Consequently, as the A5754 still melts due to the heat transfer from Ti side (Raja Kumar et al., 2021), the vaporization of Mg intensifies progressively up to 0.1 mm beam offset on Ti, and then diminishes because the A5754 side melts only slightly. The vaporized Mg forms MgO particles that settle around the melted zone area (green ring visible on Figure 3 and Figure 7).

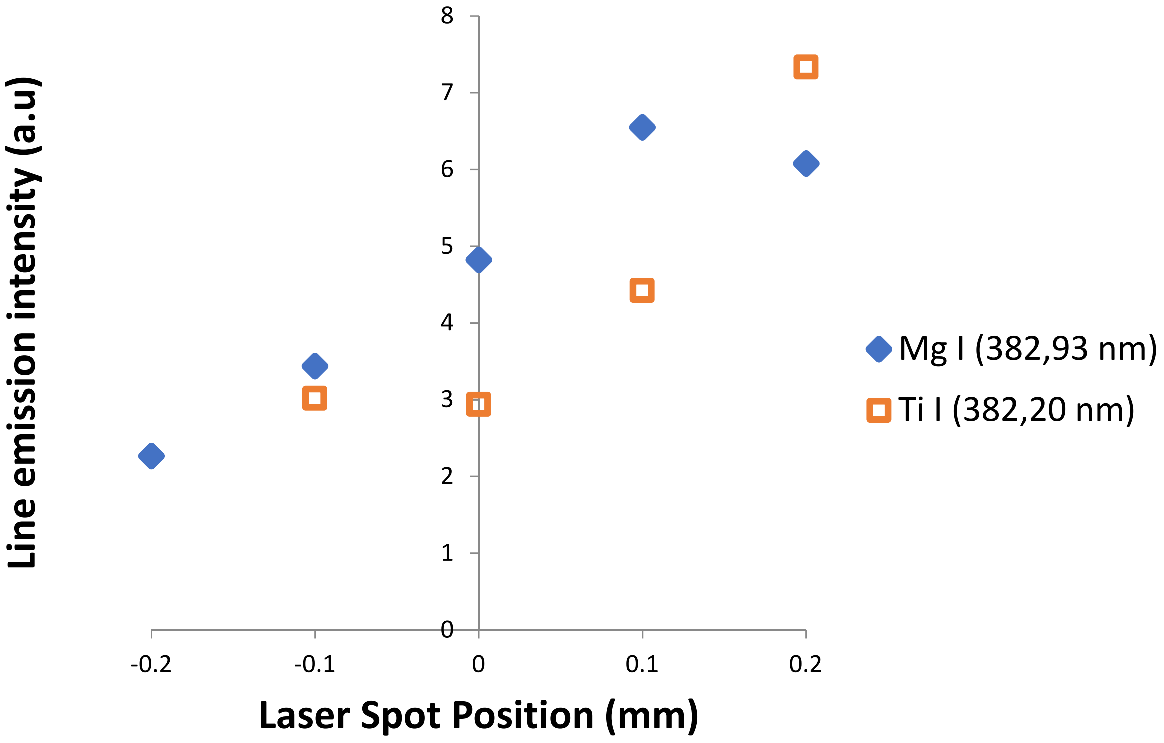

Figure 6: Observed line intensities of Mg (I) and Ti (I).

3.2 Melted zone observations

As it was observed in the previous work (Raja Kumar et al., 2021), the development of the melted zone between titanium and aluminum alloy is strongly determined by the mismatch of their physical properties. Titanium has much lower thermal conductivity and higher absorption coefficient to Yb:YAG laser radiation compared to aluminum alloy, which determines its leading role in the formation of the keyhole, but also in the development of the plume. Like in the previous work, the top view of the melted zones (Figure 7) shows the preferential ejection of the matter from the liquid zone on aluminum side, whereas the depression remaining after the closing of the keyhole is situated preferentially on titanium side. This observation is in agreement with previously proposed explanation: when titanium side of the joint reaches the vaporization temperature (superior to that of aluminum alloy), the formation of the keyhole involving both materials takes place, and a powerful inclined vapor jet from titanium side (Figure 8) induces the lateral ejection of the melt on aluminum side. With LSP displacement from titanium towards aluminum, the ejections of the melted zone on aluminum side become more pronounced, which is concordant with the observed inclination of the plume discussed in section 3.3.1.1. The variability of the impact shapes corresponding to the same LSP reflects the inherent instabilities of the keyhole and the vapor plume. The melted zones are surrounded by a ring of oxidized Mg.

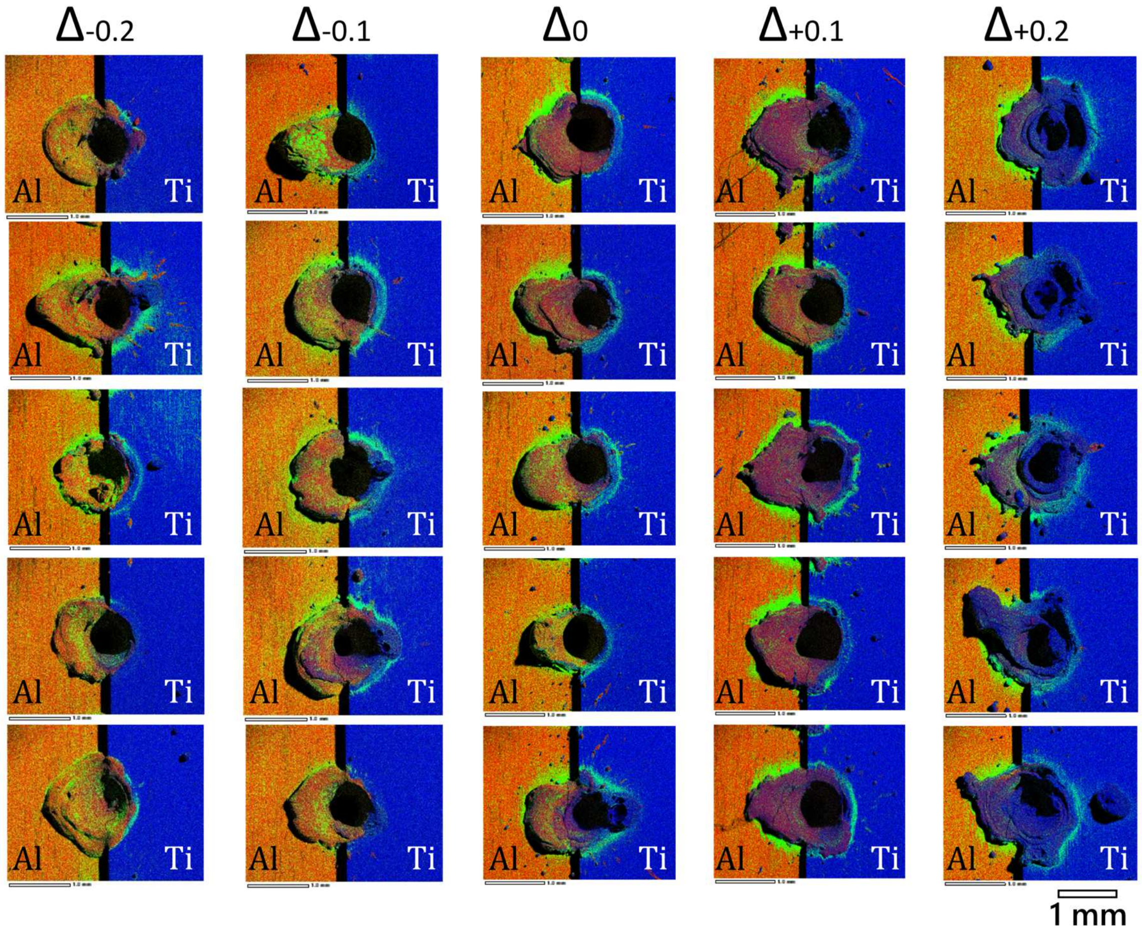

Figure 7: Elemental mapping from EDS analysis of the top view of 25 melted zones.

3.3 High-Speed Imaging

A preliminary spectral analysis carried out at low resolution (300 rev / mm grating) showed that in the region of the filter at 394 nm, the fundamental lines of Al I are observed, along with some emission lines of Ti I (Figure 4). The continuous background resulting from thermal radiation was weak. In the 810 nm region, on the contrary we do not observe spectral emission (in agreement with Kramida et al., 2020 and Kurucz, 1995 databases), but we observe thermal radiation. According to Planck's law, thermal radiation at 810 nm is 20 times greater than at 394 nm, for a vapor temperature of pure Al (2743 K) and 4.5 times greater for a vapor temperature of pure Ti (3560 K).

3.3.1 Spatial characteristics

In this section the global behavioral changes observed in the vapor plume observation especially for the two LSP's $\Delta_{-0.2}$ and Δ_0 when observed through the two filters are analyzed. Two methods of data extraction can be performed to obtain a view of the overall behavior of the vapor plume.

1. Performing the measurements on each image separately and then processing the data using averages, standard deviations, etc.
2. Directly producing the average images and then performing the measurements at the end.

Several measurements were made on the ROI for each image and their averages were calculated by LSP and λ. This method of data acquisition from every image separately and then analyzing the data provides three distinct advantages than directly producing an average image and performing the measurements at the end.

1. When using the second method, if the camera is moved relative to the LSP by even just 0.5 mm, it could lead to bad superposition of the keyholes and the plume which would lead to blurry average images and therefore producing erroneous results.
2. Also, when the average images are made from 8-bit images, the gray values are stored in integer values at each step and if multiple steps are involved in the process, this could lead to loss of critical data from the rounding of the significant figures.

3. In the first method, the data can be analyzed, and the region of high variances can be ignored, and the rest of the data can be used to perform calculations. This would not be possible if the images are averaged first. Due to the uncertainties in the actual start of the pulse and the simultaneous erratic behavior of the plume, all the following measurements (in this section: spatial characteristics) were averaged only from the interval of 0.78 ms ~ 5.47 ms.

The image treatment of the vapor plume is a tedious process because, the plume not only exhibits oscillatory behavior, but also it has a constantly changing, very irregular shape profile and size. In our previous works (Raja Kumar et al., 2021), we have used the method of approximating this irregular shape to fit an ellipse over the perimeter of the selection area. But since the shape of the selection does not always resemble an ellipse, in this work we also measure the Feret's maximum and minimum caliper, also known as Feret's diameters (suitable for size measurement of an irregular shape profile). There are several methods available to calculate the Feret's diameter which affect the speed of computation, precision, and accuracy (Dražić et al., 2016). We used the default Feret's diameter function that is available in the Fiji software.

Both methods, the Fit Ellipse and Feret's Diameter, have their advantages and disadvantages (Figure 14). For example, the Fit Ellipse function fits an ellipse over the ROI and provides the height and width of the vapor plume from the lengths of the ellipse's major and minor axes. This method of measurement does not provide easy definitions for the points between which the ellipses axes must remain and therefore introduces a degree of error in function of the size of the ROI. But upon visual analysis, it was noted the ellipses were best suited for the measurement of the angle of inclination of the selection. While the Feret's caliper measurements are well defined for size measurements, they are not desirable when the ROI takes a dumbbell-like shape or has multiple ROIs. In the end, utilizing both these methods of size measurement to understand the morphology and orientation of the vapor plume and as well as understand the shortcomings of these methods themselves in this field of research seems more logical than just choosing one over the other.

3.3.1.1 *Plume Orientation*

While the Feret's angle and Ellipse angle (angle of the major axis of the fitting ellipse) have slightly different values, the overall behavior based on LSP remain consistent for both the measures. The average ellipse angle comparisons between the filters 810 nm and 394 nm can be seen in the Figure 8 (> 0° means inclination towards Al side).

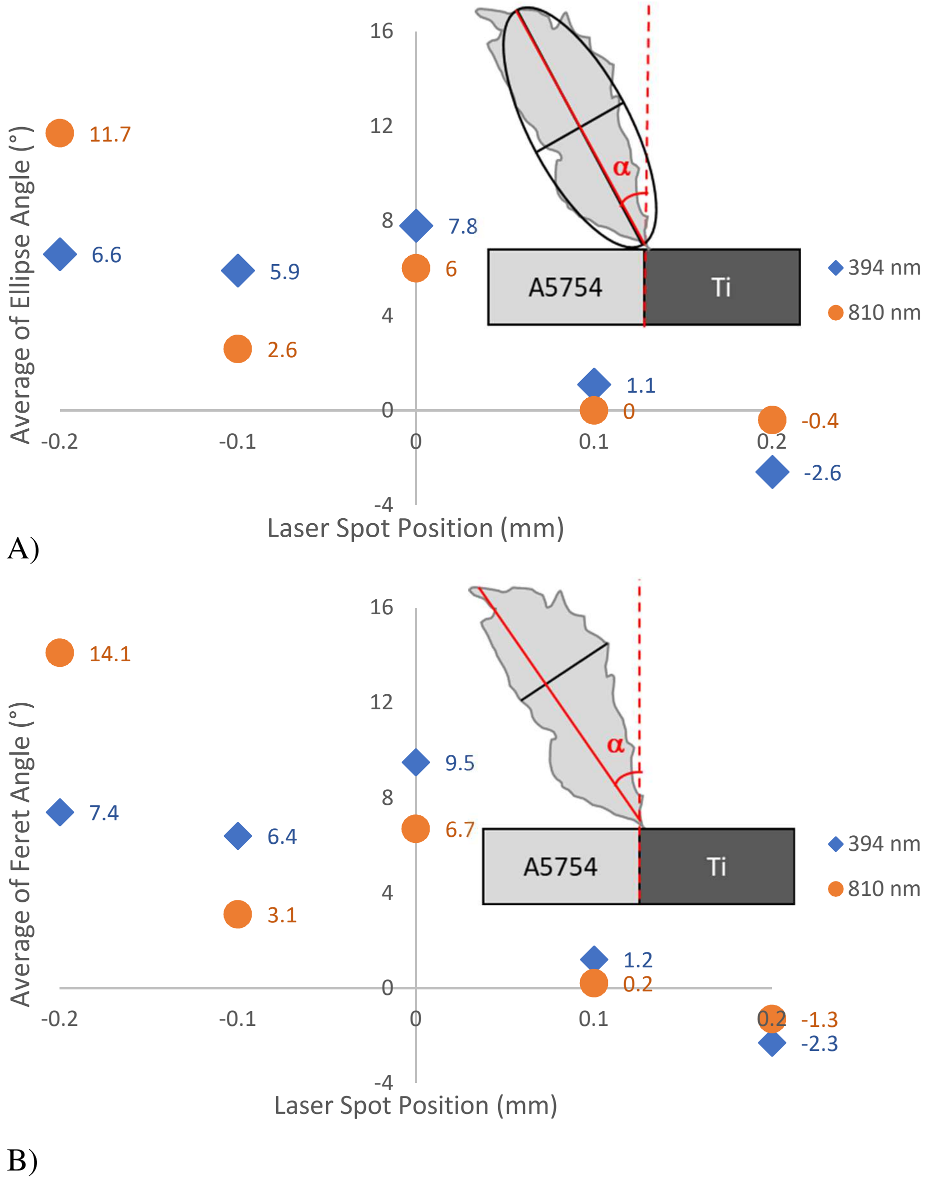

Figure 8: A) Average Ellipse Angles and B) Average Feret Angles.

For the observations made in the case of Δ_0, 810 nm images show significant reduction in inclination when compared to their counterparts at $\Delta_{-0.2}$. But the 394 nm images do not show a similar decrease. This was an interesting phenomenon and required extensive analysis to understand clearly. The LSP moved towards titanium show mostly vertical jets except in the case of $\Delta_{+0.2}$ which slightly inclines towards titanium.

3.3.1.2 Plume dimension

The overall observation of the ROI area could let us characterize the expanse of the plume. Authors relate the characteristics of the plume such as height, width, and area to complex phenomena such as the plasma properties within the vapor plume (Szymański et al., 1997), particulate matter (Zou et al., 2021) etc. But the observation of the dimensions of the plume under different wavelength regimes, is not the same. Even though the differences in the values are sometimes very small, the characteristics of the average ROI area (Figure 9) necessitate explanations since the edge selection was a rigorous process with very little room for error.

It is obvious that the 810 nm filter shows a plume of bigger surface area when compared to the 394 nm plume. This can be explained in a following way. The formation of observable bright image for a given spectral region is due to the superposition of thermal emissivity of the dense core of the plume (considered as a black body) according to Planck law with atomic and molecular emissions from the less dense outer layers of the plume. At 810 nm, the thermal emission is much more intense than for 394 nm. For example, at the vaporization temperature of Al, the ratio between the emissivities at 810 and 394 nm is about 20. On the other hand, the atomic or molecular emissions were not observed in 810 nm range. Consequently, the observation of the plume at 810 nm provides the location of Thermally Excited Regions (TER). The 394 nm spectral region is rich in emission lines of both Al I and Ti I, and the atomic emission is intense enough, taking into account the evaluated electronic temperatures of Ti I (Figure 5), whereas thermal emission is much less significant. This is the first reason why the plume area is smaller for the images obtained with 394 nm filter. As the image of the plume observed at 394 nm is mainly composed by the superposition of atomic emissions, it reflects the location of Atomically Excited Regions (AER). The second reason may be the sensitivity of the high speed camera: according to Ametek©[*], it is three times higher at 810 nm compared to 394 nm.

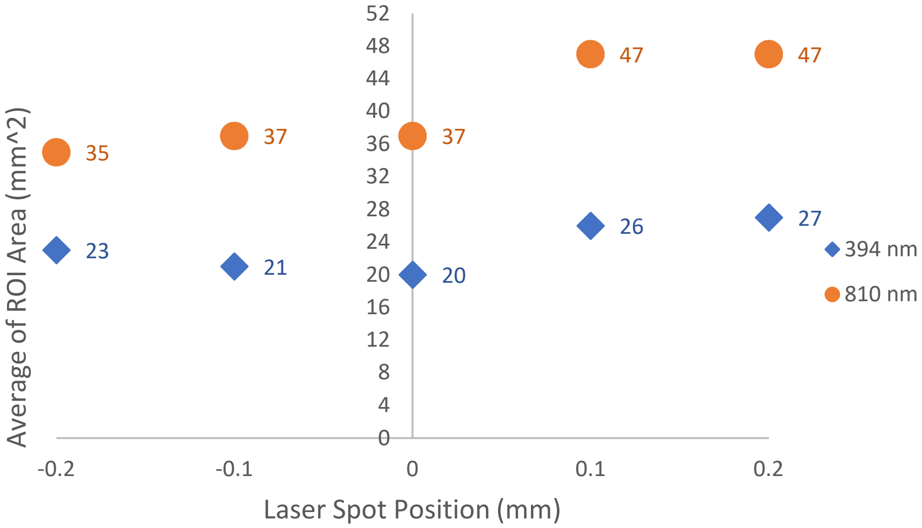

Figure 9: Average area of the AER (394 nm) and TER (810 nm) with respect to LSP.

It is not unusual that the average area for LSPs $\Delta_{+0.1}$, $\Delta_{+0.2}$ to be greater than the average areas for LSPs $\Delta_{-0.2}$, $\Delta_{-0.1}$, Δ_0 at both wavelengths, since Ti is a well-known better absorber of YAG laser radiation, easily excites atomically (Al ~ 25347 cm^{-1}, Ti ~ 7255 cm^{-1}). While the same reason can be used to explain the slight increase in the average area for the 810 nm videos when the laser spot is moved from $\Delta_{-0.2}$ to Δ_0, it is contradicting to the average area of the Atomically Excited Regions (AER) observed with the 394 nm filter, which show a slight decrease in the average area. And so, this required validation of the behavior of the ROI area, a deeper analysis of the shape of the ROI and the distribution of intensities within the ROI to understand this result.

The area of the rectangle calculated from the average values of the Feret Maximum and Minimum diameters and the lengths of the axes of the ellipses (Figure 10) with respect to the LSP and the optical filter can be compared with the area of the ROI for validation.

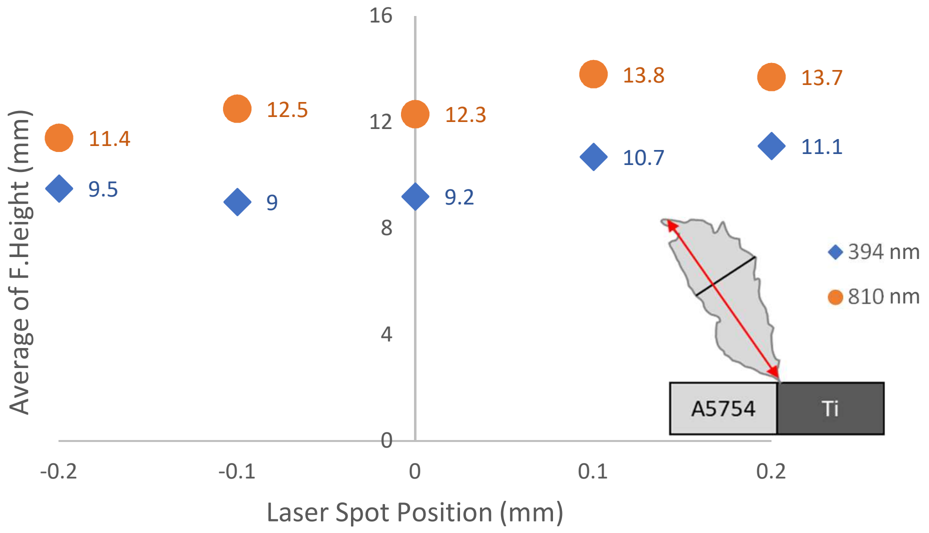
16
12
8
4
0
Average of F.Height (mm)
11.4
9.5
12.5
9
12.3
9.2
13.8
10.7
13.7
11.1
◆ 394 nm
● 810 nm
A5754
Ti
-0.2
-0.1
0
0.1
0.2
Laser Spot Position (mm)

A)

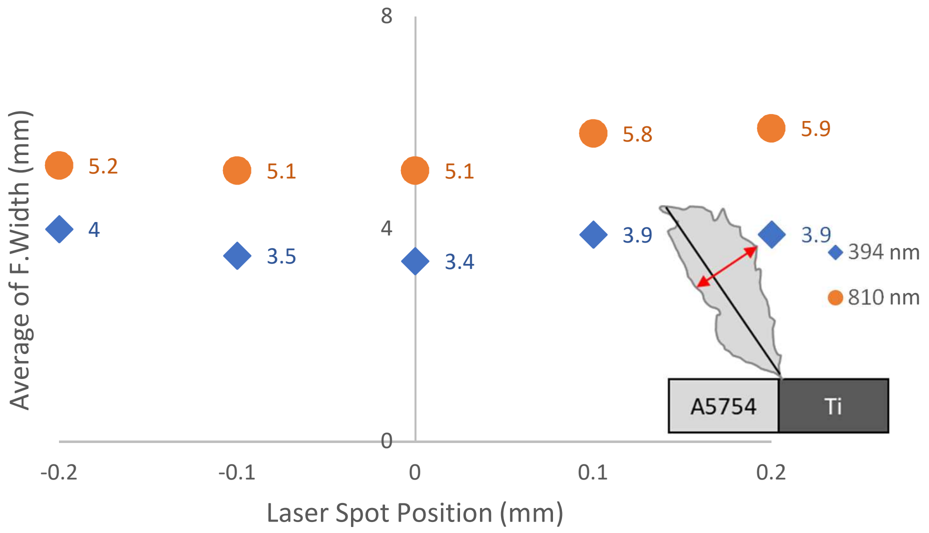
8
4
0
Average of F.Width (mm)
5.2
4
5.1
3.5
5.1
3.4
5.8
3.9
5.9
3.9
◆ 394 nm
● 810 nm
A5754
Ti
-0.2
-0.1
0
0.1
0.2
Laser Spot Position (mm)

B)

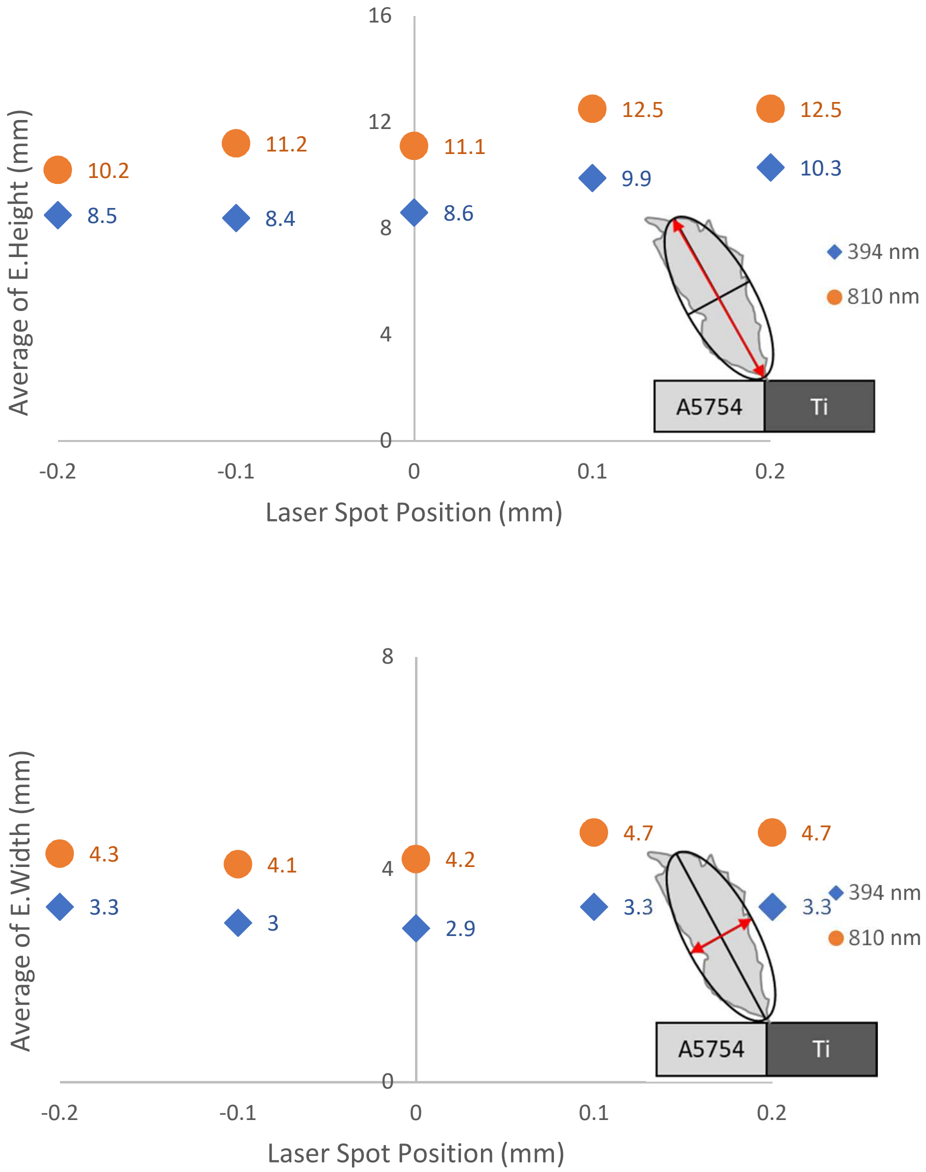

C)

D)

Figure 10: Average A) Feret's Height, B) Feret's width, C) Ellipse Height, D) Ellipse width with respect to the laser spot position.

The differences in the behavior of the average area between the optical filters for the LSPs $\Delta_{-0.2}$, $\Delta_{-0.1}$, Δ_0 when analyzed alongside calculated area of the rectangle from the height and width of the plume are presented in the Table 2. From this analysis, the following observations were made.

1. The calculated area of the rectangle is much larger than the ROI area. This is primarily due to the irregular shape of the ROI. This marks the necessity to find better

techniques to characterize this irregular plume shape rather than just using height and width.

2. The over-estimation in the calculated area of the rectangle is high also due to the large positive error in the Feret's Diameters. Positive error is a typical characteristic of Feret's diameter when it is used to study elongated particles (Walton, 1948). Since the plume is tapered near the keyhole whilst broadening with height accompanied by the varying roundness upon moving the LSP towards aluminum, such an error is unavoidable.
3. Although there is an over-estimation, only the area calculated from the Feret diameters resemble the curve matching the actual ROI (Table 2) for the optical filter 810 nm. This confirms that the Feret's diameter could be used as a complementary measure to the Fit Ellipse for verification and confirmation.
4. The decrease in ROI area for the AER when the LSP is moved from $\Delta_{-0.2}$ to Δ_0, is not a mere co-incidence or a statistical error, but it is rather confirmed with the calculated area of the rectangle which also behaves similarly. Therefore, the phenomenon of decreasing selection area should not be ignored as statistically insignificant for having small differences in values. It is the behavior of the 810 nm selection area that becomes questionable since the actual ROI area and the calculated rectangles' area do not always match the curve for the LSP moving from $\Delta_{-0.2}$ to Δ_0. This is due to the compounding of positive errors in the measurements, which create deviations in the calculated area. This effect being seen only for 810 nm represents that the TER does not conform very well to its own shape profile (during the pulse time or between different pulses) as much the AER conforms to its own.
5. The over-estimations of the calculated area depend on both the optical filter and the size of the selection area while the conformity of the ROI to the shape profile depends

on only the optical filter. If the height, width, or area of the plume were used to estimate the volume or other properties such as the plasma, particle distribution, etc., in the TER or the AER it should be noted that the uncertainties depend on the observation wavelength and the error in size and position of the plume should be used to adjust the uncertainties accordingly.

Table 2: Comparison of areas of ROI and calculated rectangles.

Optical Filter	**394 nm**			**810 nm**		
LSP	$\Delta_{-0.2}$	$\Delta_{-0.1}$	Δ_0	$\Delta_{-0.2}$	$\Delta_{-0.1}$	Δ_0
$\mathbf{Area_{ROI}}$ ($\mathbf{mm^2}$)	22.9↘	20.7↘	20.4	34.6↗	36.8↗	37.2
$\mathbf{Area\ of\ Rectangle_{Calculated}}$ ($\mathbf{mm^2}$)						
$\mathbf{HEIGHT_F * WIDTH_F}$	38.1↘	31.5↘	31.2	59.6↗	62.5↗	62.9
$\mathbf{HEIGHT_E * WIDTH_E}$	27.7↘	25.2↘	24.9	43.4↗	46.3↘	46.2
$\mathbf{HEIGHT_F * WIDTH_E}$	30.8↘	27.0↘	26.9	49.0↗	51.6↘	51.3
$\mathbf{HEIGHT_E * WIDTH_F}$	30.4↘	27.1↘	26.9	52.8↘	51.6↘	51.2

3.3.2 Distribution of Intensities

The distribution of pixel intensities can be defined through the image moments such as center of mass, centroid, and skewness. Their overall behavior with respect to the different LSPs and optical filters were studied.

In simple terms, the relative differences in the position of the centroid and the center of mass depend on the distribution of brightness/pixel intensities/gray values within the selection area. The averaged center of mass and centroid were calculated and their position in the Y-axis i.e., their vertical distance from the keyhole for each LSP with respect to the optical filter are shown in the Figure 11.

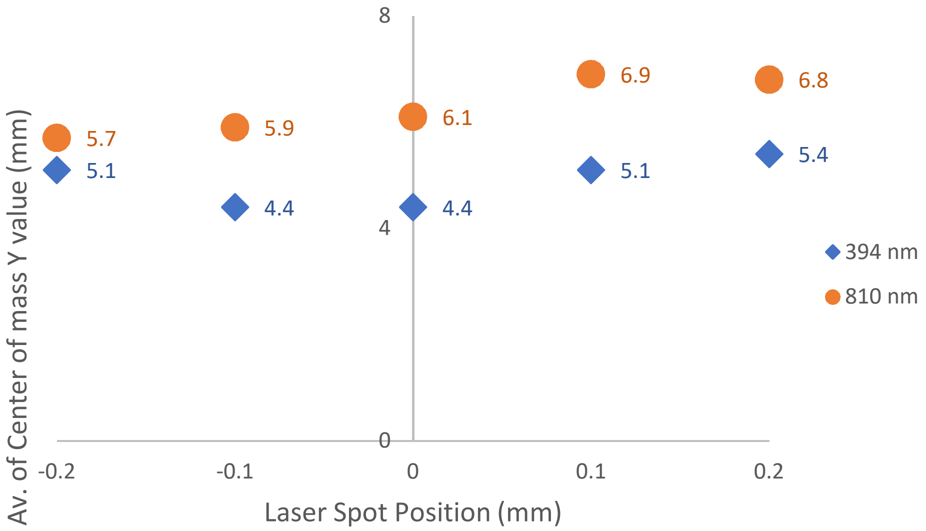

A)

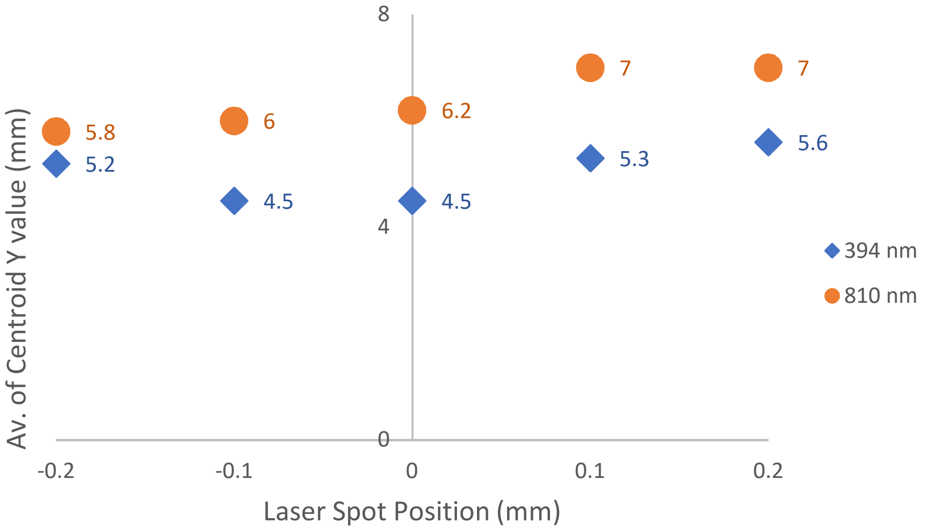

B)

Figure 11: Average Y values of A) Center of Mass and B) Centroid.

While the center of mass and centroid exhibit the same characteristics and only differ by less than 0.2 mm, comparing their values among the different LSPs between the two filters provides information about the behavior of the TER or AER. Due to the closeness in their values, instead of addressing the center of mass and centroid separately, henceforth we generalize and refer to them as Probability Zones (for ease of understanding). Probability Zones (PZ) are the places which have maximum probability for the plume to be present between 0.78 ms ~ 5.47 ms.

The reason for the naming convention behind the term "Probability Zones" is explained as follows: Common sense and numerical modeling dictates that the maximum temperature and the atomic concentrations of the vapor plume will be near the keyhole opening since the laser beam is focused to be on the plane of the metal surface (Raja Kumar et al., 2020b; Cai et al., 2018). But the highly oscillatory behavior of the plume along with its irregular shape, causes difficulties in localizing the vapor plume to an exact region or volume in space. In addition, identifying the temperature or atomic concentrations in this unlocalized space is not ideal. But the average of the centroid or center of mass calculated from every single selection can be useful in resolving this problem. Although the plume is not a rigid body, for a single image (ideal image must be captured with an exposure time less than half the time period required by the plume to change its behavior), the centroid or the center of mass represent the weighted average position of all the parts that compose it (Gahramanova, 2019). Therefore, localization of the ROI is facilitated by finding these points. For a plume that fluctuates in both orientation and size, averages of these points could let us find the most probable location for the plume to be present with the maximum intensity. And therefore, they are called Probability Zones.

Since, the centroid is more shape dependent, their slightly higher Y values compared to the center of mass indicate that the plume is narrower near the keyhole and a little wider at the top. And, when we look at the average images of the plume, it is evident that most illuminated parts of the plume lie between the PZ and the keyhole opening. We were unable to calculate reliable data on the horizontal position of the centroid because changing the optical filter had to be done manually, which leads to a displacement in the keyhole position in the image by 1 ~ 2 mm due to the movement of the camera. And so, the exact horizontal position of the centroid relative to the laser spot and the keyhole in the images could not be identified without introducing a degree of uncertainty large enough to question statistical reliability.

Since the PZs are indicators of clustering of the most intense parts of TER or AER without neglecting the overall behavior (shape, size, and orientation) of the plume, we can use their behavior to understand how changing the LSP affects the TER and AER. From the Figure 11, we can see that, LSPs on titanium have higher PZs than the others for both TER and AER due to the taller and brighter plume. For the same reasons, for LSP $\Delta_{-0.2}$, $\Delta_{-0.1}$ and Δ_0, the PZs of the TER are higher than the PZs of the AER.

While the behavior of the Y value of the PZs match with the selection area and height of the plume, the PZs of AER for LSPs $\Delta_{-0.2}$ and Δ_0 are particularly interesting. Since the behavior of AER (Y value decreases from $\Delta_{-0.2}$ to Δ_0) contradicts the behavior of the PZ of TER (Y value increases from $\Delta_{-0.2}$ to Δ_0), it leads us to make the following statements:

1. Similar contradicting behavior observed in orientation when comparing AER and TER, for the LSPs $\Delta_{-0.2}$ and Δ_0 was not an anomaly.
2. Higher % difference in the AER PZ -Y value between $\Delta_{-0.2}$ and Δ_0 when compared with the similar differences in selection area and the heights, shows that there is relatively less clustering of the maximum intensities between the PZ and keyhole in the AER of LSP $\Delta_{-0.2}$.

Visual analysis of the treated videos frame by frame was done. The reason behind the less clustering of the intense regions in AER for $\Delta_{-0.2}$ is due to the unstable nature of the plume. Till now, we have assumed that the plume was a zone of vapor continuously emitted from the keyhole which fluctuated in shape, size, and orientation. But upon visual analysis of the AER for $\Delta_{-0.2}$, we see that the plume is not a continuous zone of vapor emitting from the keyhole. It is also not just a case of plume attenuation or changes in orientation, which produces the higher PZ for LSP $\Delta_{-0.2}$, but the plume is rather extinguished completely during certain moments. The time duration when there is no plume emission from the keyhole is very short (probably ~ 150 μs) and its appearances in our videos seem random. For example, among the videos captured with the 394 nm filter for the LSP $\Delta_{-0.2}$, the number of occurrences of this extinction and the time of occurrences were not consistent. The extinction of the AER also happens in LSP $\Delta_{-0.1}$ in one of the videos at around ~ 4.8 ms. But this was not observed in the other videos for LSP $\Delta_{-0.1}$. To understand more about the occurrences happening within the AER, the original untreated videos were also analyzed visually. While the phenomenon causing this extinction is not within the scope of this article, more details relating how this extinction affects several parameters of the AER and the TER, are explained in the discussion section.

The characterizations of the plume using skewness are available in the **Supplementary data file**.

4 Discussion

In our previous work (Raja Kumar et al., 2021), we assumed that the strong Ti-rich vapor jets ejected from the keyhole wall on the titanium side, to be the cause of inclination in dissimilar welding of aluminum and titanium where all the observations were made at $\lambda = 810$ nm. To quote our own words, "The initially observed pronounced inclination (…) can be attributed to the preferential evaporation from the titanium surface". But in this present article we see why that this statement was incomplete, and that it needs refinement.

So, before defining inclination of the vapor plume, first we need to define what is being perceived as the vapor plume with the two optical filters. While the Ti-rich jets from the titanium wall for $\Delta_{-0.2}$ do exist (as mentioned in the previous work) and even if they can be the primary reason of the observed inclination, the observed object at 810 nm that we identify as the vapor plume is rather a complex mixture of Al atoms, Ti atoms, oxidized materials, air molecules and some weakly ionized Ti. This Thermally Excited Region (TER) which is observed at λ = 810 nm infrared regime, has been addressed as the vapor plume till now. But this is an incomplete picture and can lead to false conclusions. For example, the evaporation of the aluminum atoms was not very evident in our previous work. But from the visual analysis of the original untreated videos at λ = 394 nm for the same LSP $\Delta_{-0.2}$, we can see that the aluminum vaporizes indeed and that the Ti-rich jet alone is not sufficient to produce the inclined phenomenon for the AER. And this is supported by the fact that for the LSP $\Delta_{-0.2}$, only 1/6th of spot width is situated on titanium. However, there are a few difficulties in analyzing (visually or methodically) this behavior with HSI when both these elements are present in the vapor simultaneously. Spectroscopy indicates that atomic emission lines of Al (I) are too close to the Ti (I) emission lines to distinguish them separately (Figure 4), thereby making it impossible to study these emissions separately using optical filters. Adding in the turbulences caused from interaction between this hot mixture and the cold air, it is even more difficult to predict the behavior of the plume, nonetheless distinguish the different parts of the plume at certain instances.

Figure 12 shows the AER images for $\Delta_{-0.2}$ taken from different instances to show the different parts of the plume and their characteristics. From Figure 12.A, we can see from the inclination of the bright region, that this bright part is the Ti vapor jet (red) emitted strongly from the keyhole wall. And there is the diffuse region of Al atoms (yellow) which may also contain some amount of Ti. This can be confirmed by the Figure 12.B, which is the next consecutive image taken over the exposure of 120 μs, where we see that the Al atoms are easily subject to convective or turbulent forces, whereas such behavior is not seen for the Ti atoms. However, it is interesting to note that from Figure 12 (C,D,E,F), the plume envelope of Al (diameter ~ 2 mm) is much greater than Ti (diameter ~ 0.2 mm) throughout the pulse time, which may be related to the lower vaporization temperature of Al. There are also the convective effects often causing the Ti jets to curve towards the joint line due to pressure differences at the center of the plume (Figure 12.D). However, the Ti jet is not continuous, and the duration of its appearance reduces with time. The continuous high vaporization of Al is accompanied by instabilities in the keyhole, which eventually extinguish the Ti jet and then subsequently the vapor plume. This can be seen in the image Figure 12.E where the keyhole is closed and predicting the concentrations of the elements within the polygon (cyan) could not be done with HSI alone. We can see the remnants of the previously emitted vapors remain above the keyhole and that no new vapors are being emitted from the keyhole. And the vapor plume emission from the keyhole reinitiates (Figure 12.F) accompanied with the presence of a small, inclined Ti vapor jet just like the beginning of the pulse (Figure 12.A). If the remnants of the plume do not remain undiffused within the capture zone, not enough pixels are illuminated to create a selection. Even though the phenomenon of extinction of the entire vapor plume is quite short, the vaporization of Al accompanied with frequent extinction of the Ti jets causes the plume to form complex interactions with the surrounding air and therefore be unpredictable (in terms of shape, size, and orientation).

This phenomenon of plume extinction coupled with a very small and inclined Ti vapor jet causes anomalistic behavior of spectral data (Figure 6) of the LSP $\Delta_{-0.2}$. As a result, in some spectra the Ti emissions could not be detected and therefore the overall Ti (I) intensity could not be calculated for this LSP. This correlation would not be possible if the HSI of the vapor plume was performed only at $\lambda = 810$ nm.

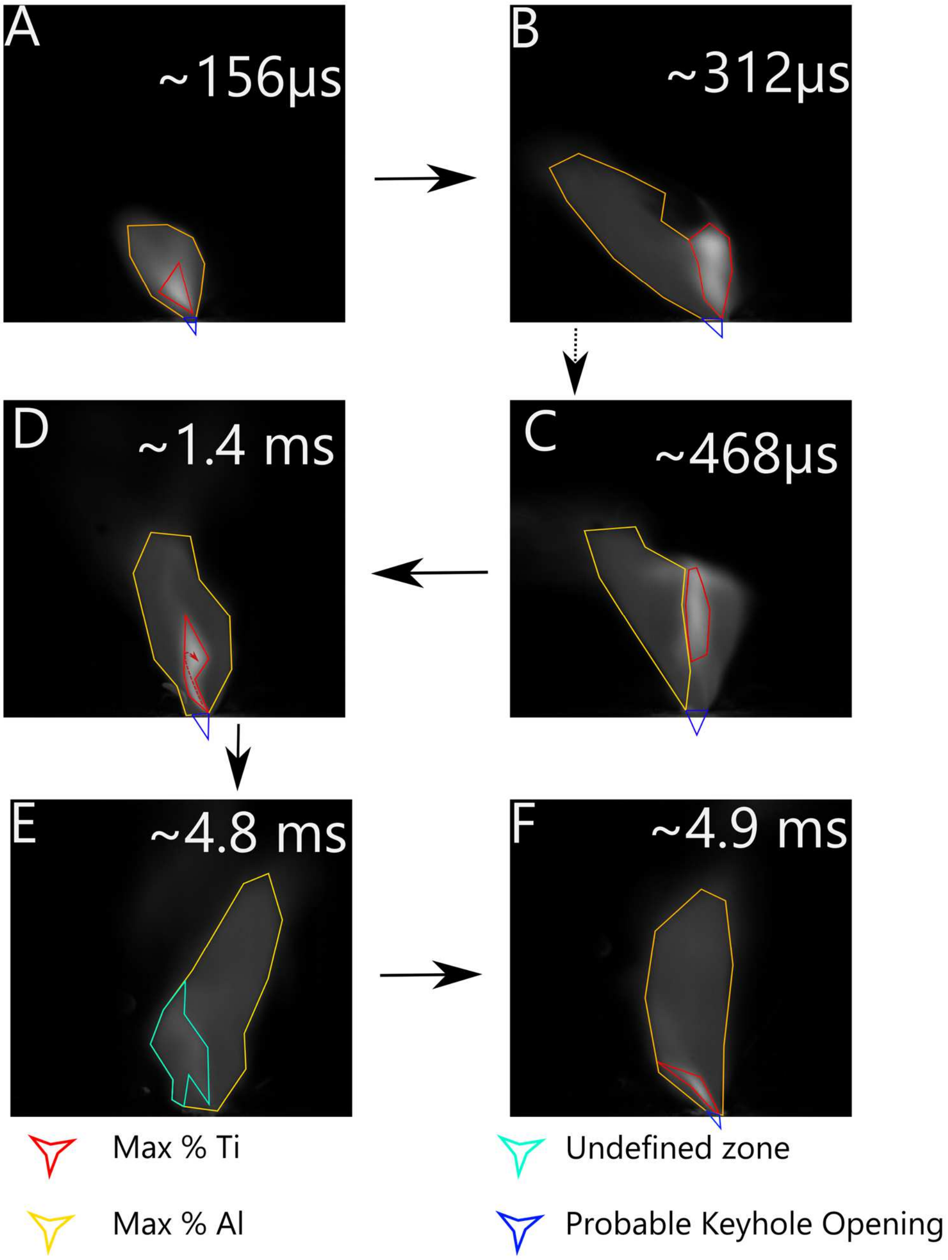

Figure 12: Images of AER for LSP $\Delta_{-0.2}$ taken at different moments.

While similar characteristics of the AER are observed for the other LSPs namely $\Delta_{-0.1}$ and Δ_0, such as the strong inclined Ti jet surrounded by Al-rich vapor (Figure 13), there are some major and minor differences. For example, the Ti jet of Δ_0 within the plume is much taller (3-4 times) and more luminous than that of $\Delta_{-0.2}$. It is also slightly wider, but this could be an effect of the diffusion under the convective velocity fields. Another difference is that this Ti jet within the Δ_0 plume is stable for longer periods of time ~3 ms before turbulence effects can take over (~ 1.2 ms for $\Delta_{-0.2}$). However, the most significant difference is that depending on the LSP, this Ti jet can either be strong and stable enough (Δ_0) to orient the AER in its direction or weak and unstable enough ($\Delta_{-0.2}$) to produce no such changes. For this reason, we can see the average angles of the TER and AER for the LSP Δ_0 are close (Figure 8). However, the differences are much larger for $\Delta_{-0.2}$ and $\Delta_{-0.1}$ because the Ti jets are not large and stable enough to influence the velocity fields in these cases (Figure 13.A). And therefore, the AER of Δ_0 is more inclined than the $\Delta_{-0.2}$ (Figure 8).

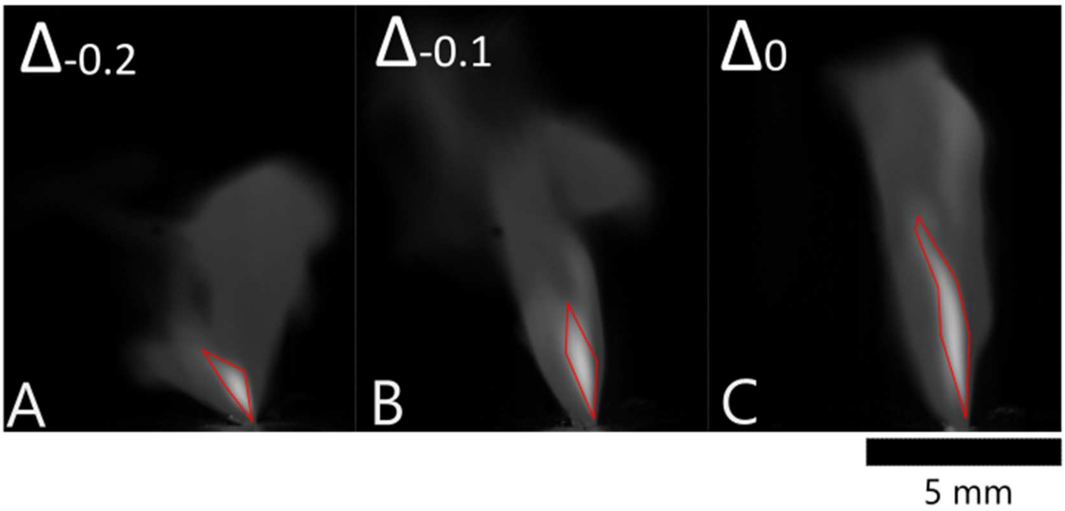

Figure 13: Concentrated Ti jets at time ~625 μs present within the AER for LSP's A) $\Delta_{-0.2}$, B) $\Delta_{-0.1}$ and C) Δ_0.

Although these Ti jets in LSP $\Delta_{-0.2}$ are relatively smaller (when compared to Δ_0) and do not influence the Al vapors' distribution, their thermal influence on the surrounding Al atoms and air molecules are not negligible. For example, let's look at the Figure 14 which is an image taken from one of the videos captured with the 810 nm filter. Figure 14.A is the original untreated TER for LSP $\Delta_{-0.2}$, whereas Figure 14.B and Figure 14.C are the normalized plumes with ROI (green), fitting ellipse (red) and the Feret diameters (purple). This is the TER which resembles the corresponding AER in Figure 13.A. And this image happens at ~0.935 ms. The small, concentrated Ti jet from AER is drawn on the Figure 14.A (red). However, the region enclosed in the white curves are slightly brighter than the rest of the plume and extend from the Ti jet. The regions surrounding this zone are hence illuminated, and this changes the entire shape and size of the plume that is being observed as the TER (compare to AER in Figure 13.A). Therefore, even if the $\Delta_{-0.2}$ Ti jet is too weak to influence the shape and size of the AER, due to thermal interactions, this weak Ti jet is hot enough to exert its thermal influence on the surrounding regions thereby causing high inclination angle values (for TER $\Delta_{-0.2}$ - Figure 8).

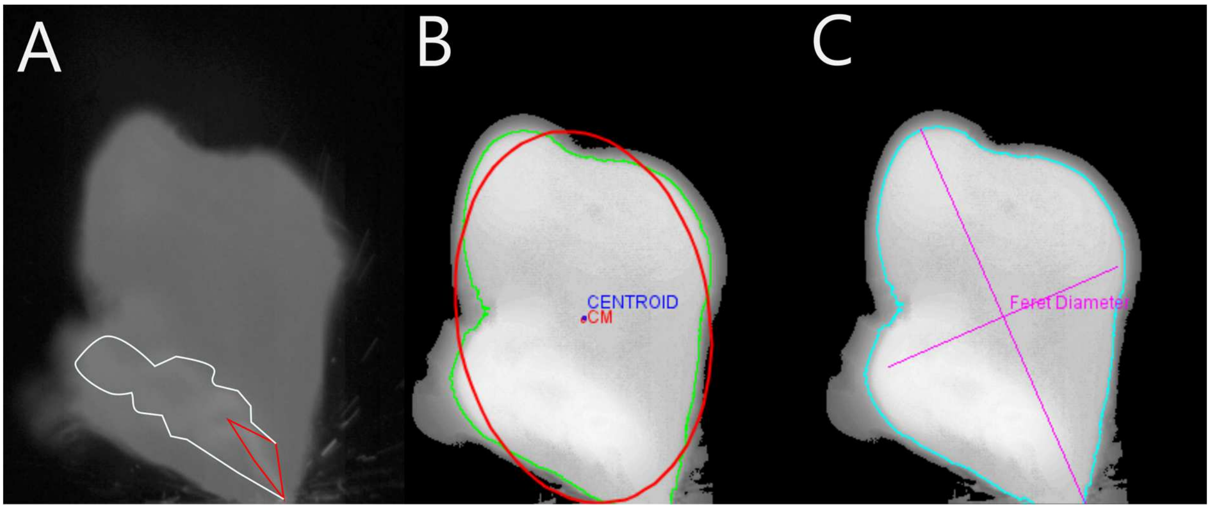

Figure 14: TER for LSP $\Delta_{-0.2}$ at ~0.935 ms A) Untreated image with Ti jet (Red) and high temperature zones (white) B) Normalized with ROI, fitting ellipse, centroid, and center of mass C) Normalized with ROI and Feret's Diameters.

To facilitate understanding this plethora of analyses, results and inferences from this work, a simple tabulation comparing the relative observations for the two LSPs $\Delta_{-0.2}$ and Δ_0, is compiled along with the explanations.

Table 3: Significant observations.

Property	**$\Delta_{-0.2}$**	**Δ_0**	**Evidenced by**	**Inference/Explanation**
Ti % in vapor	↓	↑	Spectroscopy (Figure 6)	Less incident laser power on Ti
Area of TER	↓	↑	HSI – Area (Figure 9)	Depends on % Ti in vapor.
Area of AER	↑	↓		Higher in $\Delta_{-0.2}$ due to turbulences from Al in vapor
Angle of TER	↑	↓	HSI – Angle (Figure 8)	TER surrounds Ti jets even for lesser concentrations and momentum
Angle of AER	↓	↑		Ti jets cannot dominate the entire AER when weak and unstable in $\Delta_{-0.2}$.

Vertical position of PZ for TER / High Temperature zones	↓	↑	HSI – Centroid/Center of mass (Figure 11)	Depends on the height of the Ti jet.
Vertical position of PZ for AER / Max concentration zones	↑	↓		Discontinuous plume behavior, unlocalized detached remnants of plume cause higher PZ in $\Delta_{-0.2}$.
Plume brightness	↓	↑	Spectroscopy (Figure 6)	Depends on Ti % in vapor.

Therefore, while the vapor plume is relatively stable for LSP Δ_0 in which the Ti jet from the titanium wall of the keyhole influences the size, shape, orientation, etc., of the plume, it is not the same for LSP $\Delta_{-0.2}$. The influence of Ti jets for LSP $\Delta_{-0.2}$, is only over the distribution of thermal energy within the vapor plume and the surrounding air. From spectroscopy, we know that the emission intensity is lower for $\Delta_{-0.2}$. And we see that this is caused due to the relatively small and unstable Ti jets. The instabilities are caused from the unstable Al vaporization (neither unidirectional nor stable) which not only extinguish the Ti jets, but the entire plume itself (more frequently for LSP $\Delta_{-0.2}$, rarely for $\Delta_{-0.1}$). This frequent extinction of the Ti jet and the plume, causes more turbulent effects from convection interactions with air. And therefore, the plume becomes less localized in space (higher PZ), has a larger ROI area for the AER and shows greater width for both the TER and AER.

From the results, we also see that the ellipse angle is better suited than Feret's angle for orientation calculations (Figure 8) from the fact that both TER and AER exhibit almost the same orientation for LSP Δ_0. There is no significant advantage observed between centroid or center of mass. Mean is not useful if the images must be normalized. Although Feret's diameters have higher positive errors, they are more accurate in predicting the relative variation in size of the plume than the ellipse axes.

In short, the statement in our previous work was, "The initially observed pronounced inclination (…) can be attributed to the preferential evaporation from the titanium surface" (Raja Kumar et al., 2021). But from this work, we modify it as follows:

In dissimilar laser welding of Ti/Al, the observed inclination of the plume can be attributed to the preferential evaporation from the titanium surface only if the Ti jet is continuous and stable enough, and if the plume is considered to be an envelope that contains purely the atoms/ions of the elements in the metals/alloys being welded. If the plume can be considered as a region in space that contains the atoms/ions/molecules of any element (metal, air, protective gas, etc..) which are hot enough to emit thermal radiation, the first statement does not apply because even small proportions of Ti in the vapor can affect the shape, size, and orientation of the plume considerably.

5 Conclusions

From the in-depth analysis of HSI of the vapor plume under the two wavelength regimes 810 nm and 394 nm, the morphology, orientation, and dynamics of the vapor plume were compared.

The comparative influence of titanium in size, orientation, and dynamics of the TER (vapor plume observed at 810 nm) was found to be higher than aluminum.

The AER (vapor plume observed at 394 nm) seemed to undergo frequent extinction for the LSP $\Delta_{-0.2}$ probably due to the closing of the keyhole from the instabilities produced by aluminum. This led to the formation of detached parts of the plume at greater heights which in turn led to the calculation anomalies for the area and the most probable zone for the plume to be present.

The extinction of the TER is observed less for LSP $\Delta_{-0.2}$ since air molecules and other heated matter in the vicinity are hot enough to emit light in the observed wavelength (810 nm).

The stability of the vapor plume is dependent on the amount of incident laser on the titanium surface. This leads to the supposition of a presence of a threshold below which the TER and AER do not correspond well, where the TER is influenced significantly by titanium and the AER is influenced equally by all the metals undergoing vaporization.

Intensity calculations in spectroscopy correlates well with HSI. The spectral data indicate that while the atomic excitation temperature of titanium remains consistent around 7000 K for all LSPs, the amount of vaporized material in the plume vary proportional to the amount of incident laser correspondingly.

In the methods used for treatment and analysis of images of the vapor plume, averages of values calculated from repeated experimental conditions, satisfy the underlying physics of the plume which could be observed from visual analysis of every image separately. Some anomalies are produced directly in correspondence with the instabilities and extinctions of the plume. In determining the size and orientation of the plume, both the Fitting Ellipse and Feret Diameter methods have their own advantages and drawbacks. Multi-level thresholding can be substituted instead of the traditional image treatment of the vapor plume (which usually involves Erosion/Dilation) without compromising on the data.

5.1 Perspectives

To complete the spectroscopy study, the relationship between the height of the acquisition focus and the intensity of various acquisition wavelengths could enlighten the differences between the temperature distribution and the concentration distribution within the vapor plume. Concerning HSI, further experiments using optimized acquisition parameters and higher image frequency (≥20 000 fps), comparable to that of recent experiments of Zheng et al., 2018 and Mayi et al., 2019 will be carried out next to yield more interesting results.

In order to develop deeper understanding of the effect of properties mismatch on plume behavior, the experiments in overlap configuration (Al on top or Ti on top) should be performed and compared with results available in literature (Schmalen and Plapper, 2018; Seibold et al. 2020).

Combining optimization techniques with computer vision and machine learning for HSI of the vapor plume and the melt pool in dissimilar welding while dynamically changing observation wavelength can lead to better understanding of the results in spectroscopy. And if possible, it could lead to the estimation of physical properties of metallic vapors at high temperatures when combined with numerical modelling through artificial intelligence.

Acknowledgements

This research was funded by the Regional Council of Bourgogne Franche-Comté, the Graduate School EIPHI (Contract ANR-17-EURE-0002) and the FEDER.

References

Awcock, G. J. & Thomas, R. 1995. Applied Image Processing. Palgrave, London. https://doi.org/10.1007/978-1-349-13049-8

Cai, Y., Heng, H., Li, F. & Wang, M. 2018. The influences of welding parameters on the metal vapor plume in fiber laser welding based on 3D reconstruction. *Optics and Laser Technology* 107, 1-7. https://doi.org/10.1016/j.optlastec.2018.05.016

De, S., Bhattacharya, A., Mondal, S., Mukhopadhyay, A., Sen, S. 2018. Investigation of flame behavior and dynamics prior to lean blowout in a combustor with varying mixedness of reactants for the early detection of lean blowout. *International Journal of Spray and Combustion Dynamics* 11, 1-20. https://doi.org/10.1177/1756827718812519.

Dražić, S., Sladoje, N. & Lindblad, J., 2016. Estimation of Feret's diameter from pixel coverage representation of a shape. *Pattern Recognition Letters* 80, 37-45. https://doi.org/10.1016/j.patrec.2016.04.021.

Fabbro, R., Slimani, S., Doudet, I., Coste, F., Briand, F. 2006. Experimental study of the dynamical coupling between the induced vapour plume and the melt pool for Nd-Yag CW laser welding. *Journal of physics D: Applied physics* 39(2) 394-400. https://doi.org/10.1088/0022-3727/39/2/023

Farrell, D. A., Woodbury, A. D. & Sudicky, E. A. 1994. The 1978 Borden tracer experiment: Analysis of the spatial moments. *Water Resources Research* 30(11), 3213-3223. https://doi.org/10.1029/94WR00622

Gahramanova, A. 2019. Locating Centers of Mass with Image Processing Locating Centers of Mass with Image Processing. *Undergraduate Journal of Mathematical Modeling* 10(1). https://doi.org/10.5038/2326-3652.10.1.4906

Gao, M., Chen, C., Hu, M., Guo, L., Wang, Z., Zeng, X. 2015. Characteristics of plasma plume in fiber laser welding of aluminum alloy. *Applied Surface Science* 326, 181–186. https://doi.org/10.1016/j.apsusc.2014.11.136

Huang, Y., Shen, C., Ji, X., Li, F., Zhang, Y., Hua, X. 2020. Correlation between gas-dynamic behaviour of a vapour plume and oscillation of keyhole size during laser welding of 5083 Al-alloy. *Journal of Materials Processing Technology* 283, 116721. https://doi.org/10.1016/j.jmatprotec.2020.116721

Kaplan, A. F. H. & Powell, J. 2011. Spatter in laser welding. *Journal of laser Applications* 23(3), 032005. https://doi.org/10.2351/1.3597830

Kramida, A., Ralchenko, Y. & Reader, J. 2020. *NIST Atomic Spectra Database (version 5.9).* https://dx.doi.org/10.18434/T4W30F

Kurucz, R. L., 1995. The Kurucz (Smithsonian) Atomic and Molecular Database. *Highlights of Astronomy 10*, 579-579. https://dx.doi.org/10.1017/S1539299600012119

Levesque, M. P. & Buteau, S., 2007. Image processing technique for automatic detection of satellite streaks. *Technical Report DRDC Valcartier TR 2005-386, February 2007.* https://apps.dtic.mil/sti/citations/ADA596420

Li, J., Lui, Y., Tao, Y., Zhang, Q., Kang, K., Sun, Q., Sun, Q. 2021. Analysis of vapor plume and keyhole dynamics in laser welding stainless steel with beam oscillation. *Infrared Physics and Technology* 113(2), 103536. https://doi.org/10.1016/j.infrared.2020.103536

Mayi, Y.A., Dal, M., Peyre, P., Bellet, M., Metton, C., Moriconi, C., Fabbro, R.2020.Laser-induced plume investigated by finite element modelling and scaling of particle entrainment in laser powder bed fusion. Journal of Physics D: Applied Physics 53(7),075306. https://doi.org/10.1088/1361-6463/ab5900

Mohanta, A., Lanfant, B., Leparoux, M. 2019. In-situ optical emission spectroscopic investigation of direct laser melting process during fabrication of Ti-6Al-4V parts. *Lasers in Manufacturing Conference 2019, June 24-27, Munich, Germany. https://www.wlt.de/lim/Proceedings2019/data/PDF/Contribution_265_final.pdf*

Otsu, N., 1979. A threshold selection method from gray-level histograms. *IEEE transactions on systems, man, and cybernetics* 9(1), 62-66. https://doi.org/10.1109/TSMC.1979.4310076

Peuker, J. M., Lynch, P., Krier, H. & Glumac, N. 2013. On ALO emissioin spectroscopy as a diagnostic in energetic materials testing. *Propellants Explosives, Pyrotechnics* 38(4), 577-585. https://doi.org/10.1002/prep.201200144

Raja Kumar, M., Jouvard, J. M., Tomashchuk, I. & Sallamand, P. 2020a. Vapor plume and melted zone behavior during dissimilar laser welding of titanium to aluminum alloy. *Proceedings of the Institution of Mechanical Engineers, Part L: Journal of Materials: Design and Applications* 234(5), 681-696. https://doi.org/10.1177/1464420720907936

Raja Kumar, M., Tomashchuk, I., Jouvard, J.-M. & Duband, M. 2020b. A first approximation to the modeling of vapor plume evolution in laser welding. *Comsol Conference 2020 Europe, Virtual Edition, October 14–15, 2020.* https://www.comsol.fr/paper/a-first-approximation-to-the-modeling-of-vapor-plume-evolution-in-laser-welding-94431

Raja Kumar, M., Tomashchuk, I., Jouvard, J.-M. & Duband, M. 2021. Vapor plume behavior during a standalone laser pulse on the dissimilar aluminum / titanium interface : high-speed imaging with 810 nm band-pass filter. *Lasers in Manufacturing Conference 2021, Munich, Germany. June 21 - 24, 2021.*

Schindelin, J., Arganda-Carreras, I., Frise, E. et al. 2012. Fiji: an open-source platform for biological-image analysis. *Nature Methods* 9, 676–682. https://doi.org/10.1038/nmeth.2019

Schmalen, P. & Plapper, P. 2018. Spectroscopic studies of dissimilar Al-Cu laser welding. *Manufacturing Science and Engineering Conference MSEC 2018, June 18-22, 2018. Texas, USA.*

Seibold, M., Friedmann, H., Schricker, K. & Bergmann, J. P. 2020. Process control by real-time pulse shaping in laser beam welding of different material combinations. *Procedia CIRP 94*, 769-774. https://doi.org/10.1016/j.procir.2020.09.137

Shcheglov, P. Y., Gumenyuk, A.V., Gornushkin, I.V., Rethmeier, M., Petrovskiy, V.N. 2013. Vapor-plasma plume investigation during high-power fiber laser welding. *Laser Physics,* 23(1), 1-7. https://doi.org/10.1088/1054-660X/23/1/016001.

Surmick, D. M. & Parigger, C. G. 2017. Self-absorbed Al lines in laser-induced plasma. *Journal of Physics: Conference Series* 810(1), 012054. https://doi.org/10.1088/1742-6596/810/1/012054

Sunghyun, C., Matsushita, Y. & Lee, S. 2007. Removing non-uniform motion blur from images. *2007 IEEE 11th Internation Conference on Computer vision, 14-21 Oct. 2007, Rio de Janeiro, Brazil.* https://doi.org/10.1109/ICCV.2007.4408904

Szymański, Z., Kurzyna, J. & Kalita, W. 1997. The spectroscopy of the plasma plume induced during laser welding of stainless steel and titanium. *Journal of Physics D: Applied Physics* 30(22), 3153-3162. https://doi.org/10.1088/0022-3727/30/22/014.

Walton, W. H. 1948. Feret's Statistical Diameter as a Measure of Particle Size. *Nature* 162(4113), 329. https://doi.org/10.1038/162329b0

Zheng, H., You, W., Yinkai, X., Shengkun, Y., Rui, H., Yulong, G., Lihui, L., Shuili, G., Huaixue, L. 2021. Observation of Vapor Plume Behavior and Process Stability at Single-Track and Multi-Track Levels in Laser Powder Bed Fusion Regime. *Metals* 11(6), 937. https://doi.org/10.3390/met11060937

Zou, J., Han, X., Zhao, Y., Wu, Q., Xiao, R. 2021. Investigation on plume formation during fiber laser keyhole welding based on in-situ measurement of particles in plume. *Journal of Manufacturing Processes* 65, 153-160. https://doi.org/10.1016/j.jmapro.2021.03.030